Large-scale synthesis and enhanced visible-light-driven photocatalytic performance of hierarchical Ag/AgCl nanocrystals derived from freeze-dried PVP–Ag+ hybrid precursors with porosity

Deliang Chen [a,b,*], Minna Liu [a], Qianqian Chen [a], Lianfang Ge [a], Bingbing Fan [a], Hailong Wang [a], Hongxia Lu [a], Daoyuan Yang [a], Rui Zhang [a,c], Qishe Yan [d], Guosheng Shao [b,e], Jing Sun [f], Lian Gao [f]

[a] *School of Materials Science and Engineering, Zhengzhou University, 100 Science Road, Zhengzhou 450001, PR China*
[b] *UK-China Centre for Multi-functional Nanomaterials, Zhengzhou University, Zhengzhou 450001, PR China*
[c] *Zhengzhou Institute of Aeronautical Industry Management, University Centre, Zhengdong New District, Zhengzhou 450046, PR China*
[d] *School of Chemistry and Molecular Engineering, Zhengzhou University, 100 Science Road, Zhengzhou 450001, PR China*
[e] *Institute for Renewable Energy and Environmental Technology, University of Bolton, Bolton BL3 5AB, UK*
[f] *The State Key Laboratory of High Performance Ceramics and Superfine Microstructure, Shanghai Institute of Ceramics, Chinese Academy of Sciences, Shanghai 200050, PR China*

ABSTRACT

To achieve high-performance, hierarchical plasmonic Ag/AgCl photocatalysts, a freeze-drying route was developed to form porous PVP–Ag+ hybrid compounds, which were then transformed to hierarchical Ag/AgCl nanocrystals through a liquid–solid precipitation reaction followed by a partially photoreduction under ambient conditions. The PVP–Ag+ hybrid precursors and their final Ag/AgCl nanocrystals obtained were characterized by various techniques. The hierarchical Ag/AgCl nanocrystals obtained had an apparent size range of 156 ± 50 nm, and the surfaces of the large particles were covered with small nanocrystals with sizes of 33 ± 12 nm. The photocatalytic performance of the hierarchical Ag/AgCl nanocrystals was estimated by degradating organic dyes (i.e., RhB, MO, and MB) and alcohols (i.e., methanol and isopropanol) under visible light ($\lambda \geq 420$ nm) and sunlight. The results indicated that the hierarchical Ag/AgCl nanocrystals obtained were efficient visible-light-driven photocatalysts in decomposing organic dyes, and their RhB photodegradation rates (~ 0.97 min^{-1}) was ~ 54 times higher than that (~ 0.018 min^{-1}) of TiO$_2$ (P25) nanocrystals under the same visible-light conditions. The photodegradation efficiency of methanol and isopropanol reached $\sim 45\%$ and 35%, respectively, after visible-light irradiation for 60 min according to the COD data. The enhancement in visible-light-driven photodegradation performance results from the high absorbance through 350–800 nm due to the SPR effect of metal Ag species embedded in the hierarchical AgCl host nanocrystals. The influencing factors and possible growth mechanism of the Ag/AgCl nanocrystals were investigated, and the PVP molecules and the freeze-drying process were highly influenced the size and morphology of Ag/AgCl nanocrystals. The outstanding advantage of the freeze-drying assisted route is its ability in large-scale synthesis of hierarchical Ag/AgCl nanocrystals.

© 2013 Elsevier B.V. All rights reserved.

1. Introduction

Development of functional nanomaterials for energy and environmental utilization has become one of key research topics for scientists in chemistry and materials science in recent decades [1–5]. Since Fujishima and Honda discovered the photocatalytic splitting of water on TiO$_2$ electrodes in 1972 [6], semiconductor photocatalysts have attracted increasing attention as a promising technology with tremendous potentials in environmental applications, such as water disinfection, air purification, and hazardous waste remediation [7–9]. Inorganic photocatalysts based on transient metal oxide semiconductors usually have many advantages, including good biological and chemical inertness, strong oxidizing power, low cost, non-toxicity and long-term stability against photo-corrosion and chemical corrosion [6,7]. However, the wide bandgap energies and low-efficiency in charge separation limit their applications driven by solar energy [5,7,8]. For transient metal oxide semiconductors with a wide bandgap, elemental doping can

* Corresponding author at: School of Materials Science and Engineering, Zhengzhou University, 100 Science Road, Zhengzhou 450001, PR China.
Tel.: +86 371 67781046; fax: +86 371 67781593.
E-mail addresses: dlchen@zzu.edu.cn, dlchennano@hotmail.com (D. Chen).

introduce doping levels, which can absorb more energy in visible light [10–19]. But the complicated synthetic processes with limited enhancement in visible-light utilization lose their charm in large-scale applications in environmental purification.

Metal/semiconductor hybrid nanostructures are recently developed novel photocatalysts (i.e., plasmonic photocatalysts) with important applications in environmental purification and solar-energy utilization [20,21]. Some metal nanoparticles (e.g., Au, Ag, Pt and Cu) can strongly absorb UV–vis light, especially the visible light in a large wavelength range, due to their surface plasmon resonances (SPRs) property [22–32]. The typical (Au, Ag)@TiO_2 hybrid systems have been extensively investigated both in scientific aspects and practical applications [26–31]. In these systems, the nanoscale metal species are usually grown by post-treatment processes (e.g., photoinduced reduction, deposition–precipitation (DP) method, etc.) on the surfaces of TiO_2 nanoparticles [27–30]. Although these metal/semiconductor hybrid nanostructures exhibit unique SPR properties, the processes for the post-growth of metal nanoparticles on a heterogeneous host are tedious. In addition, the distribution and microstructures of the interfaces between the metal species and semiconductors are difficult to finely control.

AgCl and Ag_3PO_4 are semiconductors containing Ag^+ ions, which are convenient to grow Ag/AgCl or Ag/Ag_3PO_4 plasmonic hybrid photocatalysts by partially reducing themselves' Ag^+ ions [33,34]. Since Huang et al. [35] reported Ag/AgCl powders as a plasmonic photocatalyst, the investigations on silver halides decorated with silver species have attracted increasing attention, including Ag/AgX (X = Cl [36], Br [37,38], I [39]), and their related composite nanostructures combined with TiO_2 [40–45], WO_3 [46], H_2WO_4 [47,48], graphene [34,49–51], and so on [52]. The size and morphology of the Ag/AgCl particles strongly influence their photocatalytic activity under visible-light conditions [53]. To control the morphologies and reduce the sizes of the Ag/AgCl photocatalysts, scientists have been trying their best to explore efficient synthetic strategies, including ion-exchanging methods [35], sonochemical methods [53], microwave synthesis [54], microemulsions [55,56], solvothermal methods [57], sacrificial salt-crystal-template (SCT) route [58], solid-state reaction [59], etc. [60,61]. Though Ag/AgCl samples with morphologies of nanocubes [53,56,61,62] and cubic cages [55] have been successfully synthesized, it is still full of challenges to realize large-scale synthesis of Ag/AgCl nanocrystals with small sizes and controlled microstructures, due to the rapid growth kinetics between the silver and the chloride ions. Further depth exploration is deserved to develop effective and simple approaches toward hierarchical Ag/AgCl nanocrystals with controlled morphology and high-performance in environmental purification.

Freeze drying is an effective way to obtained porous materials with unique morphology [63–72]. The action principle of the freeze-drying process involves that a sample is frozen and dehydrated under reduced pressure, forcing the water within the sample to sublimate directly into the gas phase [63]. This procedure has been widely used in biological analysis [64], food industry [65], aerogels [66,67], biofoams [68], amorphous materials [69], core-shell structures [70], and other nanoscale materials [71]. By quickly freezing the sample, the formation of large ice crystals can be prevented, and porous structures can be expected after removing the small ice crystals, which are the templates [63,68,72,81]. The freeze-drying process is therefore a nice choice to form porous inorganic–organic hybrids from their homogeneous solutions.

In this work, we combine the freeze-drying process with photoreduction to synthesize hierarchical Ag/AgCl hybrid photocatalysts in a controlled and large-scale way. The essential points of this freeze-drying approach toward hierarchical Ag/AgCl nanocrystals involve three steps: (i) preparation of porous PVP–Ag^+ organic-inorganic hybrid precursors via the freeze-drying process, (ii) formation of hierarchical AgCl nanocrystals by direct reaction between porous PVP–Ag^+ solid precursors and Cl^- aq. solutions, and (iii) conformal transformation of the as-obtained AgCl nanocrystals to hierarchical Ag/AgCl hybrid photocatalysts by photoreduction. The factors influencing the sizes and morphologies of the Ag/AgCl samples and their related mechanisms have been systematically investigated. The photocatalytic performance of the hierarchical Ag/AgCl nanocrystals has been evaluated using organic dyes (e.g., rhodamine B, methylene blue and methyl orange) and alcohols (i.e., methanol and isopropanol) as the model substances under visible-light irradiation ($\lambda \geq 420$ nm) with various illumination intensities (50–400 mW cm^{-2}). The key roles of the freeze-drying process in the controlled synthesis of hierarchical Ag/AgCl nanocrystals and its effects on the photocatalytic performance have been emphasized.

2. Materials and methods

2.1. Chemicals and reagents

Silver nitrate ($AgNO_3$, analytically pure, Tianjing Kermel Chemical Reagent Co. Ltd.), polyvinylpyrrolidone K30 (PVP, Sinopharm Chemical Reagent Co. Ltd.), polyethylene glycol (PEG 4000, Sinopharm Chemical Reagent Co. Ltd.), sodium chloride (NaCl, analytically pure, Luoyang Chemical Reagent Plant) and ethanol (analytically pure, Tianjing Fuchen Chemical Reagent Plant) were used as received without additional purification. Organic dyes of methyl orange (MO, analytically pure, Tianjin Kemiou Chemical Reagent Co., Ltd.), rhodamine B (RhB, analytically pure, Tianjin Kaitong Chemical Reagent Co., Ltd.) and methylene blue (MB, analytically pure, Tianjin Huadong Reagent Factory) were used as the target substances to evaluate the photodegradation performance of the as-obtained samples. De-ionized water was used in all the experiments.

2.2. Synthesis of hierarchical Ag/AgCl nanocrystals

Hierarchical Ag/AgCl nanocrystals were synthesized through a simple freeze-drying route, as shown in Fig. 1. The synthesis involved three steps: (1) to synthesize porous PVP–Ag^+ hybrid precursors by freeze-drying ethanol–H_2O solutions containing $AgNO_3$ and PVP species, (2) to form AgCl nanocrystals by adding a NaCl aq. solution to the above porous PVP–Ag^+ hybrid precursors, and then (3) to synthesize Ag/AgCl nanocrystals by partially photoreducing the as-obtained AgCl suspensions.

Typically, 5.6 mL of $AgNO_3$ aq. solution (0.5 mol L^{-1}) was firstly added to 11.2 mL of ethanol containing 0.0155 g of PVP (0.14 mmol of repetitive units, C_6H_9NO) under magnetic stirring. After a stirring of 2 h, 13.2 mL of H_2O was added to the above PVP–Ag^+ solution. The ethanol–H_2O mixture of PVP–Ag^+ species was frozen at −40 °C for 30 min to form an iced solid, and the as-obtained solid was then treated in a vacuum tank at 28 °C/80 Pa for 8 h to form a porous PVP–Ag^+ hybrid precursor as solid powders. The freeze-drying treatment was performed on the vacuum freeze-drying machine (LG-1.0, Shenyang Aerospace Xinyang Frozen Equipment Manufacturing Co., Ltd., China). A NaCl aq. solution (16.8 mL, 0.5 mol L^{-1}) was then added drop wise to the above PVP–Ag^+ precursor under magnetic stirring, and a milky suspension was immediately formed upon addition of Cl^- ions. The milky suspension was stirred for another 1 h in dark, and then was irradiated under a Xe lamp ($\lambda \geq 420$ nm, 400 mW cm^{-2}) for 30 min to form Ag/AgCl nanocrystals. The Ag/AgCl sample was collected by centrifugation, washed with de-ionized water and ethanol for six times, and dried at room temperature in dark for 12 h. For purposes of comparison, Ag/AgCl samples with various molar PVP-to-Ag^+ ratios ($R_{PVP/Ag}$ = 0, 0.05, 0.5,
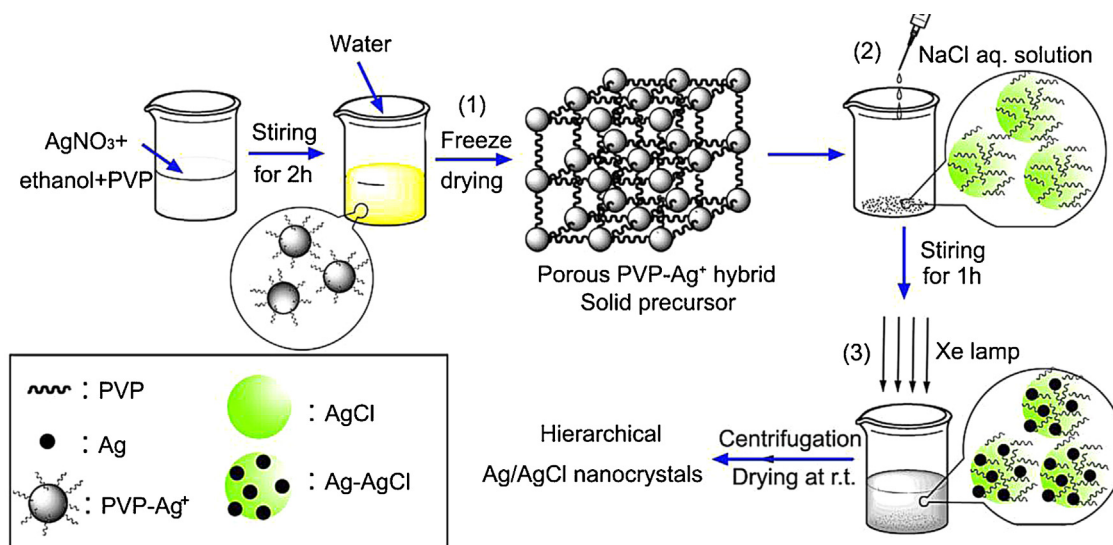
Fig. 1. A schematic diagram for the synthesis hierarchical Ag/AgCl nanocrystals via a freeze-drying route.

4) and photoreduction times (t_r = 0, 30, 60 min) were synthesized using the similar freeze-drying route. The samples synthesized via the freeze-drying route with PVP were denoted as FR_xPVP_y, and $x = t_r$, $y = R_{PVP/Ag}$ (Table S1, ESI).

Ag/AgCl samples with PEG were synthesized using the same process just by replacing PVP with PEG, and the molar PEG-to-Ag$^+$ ratio was 0.05. The Ag/AgCl sample by a direct precipitation method without freeze drying was also synthesized. Typically, 5.6 mL of AgNO$_3$ aq. solution (0.5 mol L^{-1}) was firstly added to 11.2 mL of ethanol containing 0.0155 g of PVP (0.14 mmol of repetitive units) under magnetic stirring. After a stirring of 2 h, 13.2 mL of H$_2$O was added to the above PVP–Ag$^+$ solution, and then 16.8 mL of NaCl aq. solution (0.5 mol L^{-1}) was added drop wise to the above PVP–Ag$^+$ solution. The following process was the same to the case of freeze-drying route. The as-obtained sample was denoted as $PR_{30}PVP_{0.05}$ (Table S1, ESI).

2.3. Characterization of hierarchical Ag/AgCl nanocrystals

The crystalline phases of the hierarchical Ag/AgCl samples were identified by X-ray diffraction (Beijing Purkinje General Instrument Co., Ltd., China) with a Cu Kα radiation (λ = 1.5406 Å) under a voltage of 36 kV and a current of 20 mA, with a scanning rate of 4° min^{-1} in 2θ = 20–90°. The morphology and particle sizes of the Ag/AgCl samples were observed on a field emission scanning electron microscope (JEOL, JSM-7001F, Japan), and the samples were coated with a Pt film before measurement using a coater (JEOL, JFC-1600, Japan) with coating parameters of 30 mA for 60 s. The X-ray photoelectron spectroscopy (XPS) spectra were performed on a multipurpose XPS spectroscope (Shimadzu Axis-Ultra DLD, Japan) with a focused monochromatized Al-Kα radiation (1486.6 eV). The UV–vis diffuse reflectance spectra were recorded on a UV–vis–NIR spectrophotometer (Shimadzu, UV-3600) in a wavelength range of 250–800 nm.

### 2.4. Photocatalytic test of Ag/AgCl nanocrystals

Photocatalytic degradation activity of the Ag/AgCl nanocrystals was firstly evaluated by photo-induced decomposing organic dyes (i.e., methyl orange (MO), rhodamine B (RhB), and methylene blue (MB)) under sunlight and artificial visible-light (λ ≥ 420 nm) provided by a 300 W Xe lamp (NBeT, HSX-F300) equipped with an ultraviolet cutoff filter. The light density (50–400 mW cm^{-2}) could

be controlled by changing the distance between the lamp and solution surface of photodegradation system, and the light density was measured using a light meter (Tenmars TM-208, USA).

All the photocatalytic experiments were conducted under ambient conditions with a photocatalyst concentration of 0.5 g L^{-1}. Typically, 25 mg of Ag/AgCl catalysts was firstly dispersed in a 100 mL beaker containing 45 mL of water under magnetic stirring, followed by sonication for 3 min. Secondly, the above suspension was moved to a dark condition, and 5 mL of 100 mg L^{-1} RhB aqueous solution was carefully added. The dye-containing suspension was kept magnetically stirring in dark for 30 min to reach a dye–absorption equilibrium on the surfaces of photocatalysts. The suspension with photocatalysts and dye molecules was exposed to visible-light irradiation. Aliquots of solutions (3 mL) were drawn from the reaction system by using a syringe at given degradation durations. The sampled suspensions were centrifuged at 7000 rpm for 6 min to remove the solid photocatalyst particles completely, and the upper clear solutions were then transferred to a quartz cuvette for measuring their absorption spectra in the wavelength range of 300–800 nm using a UV–vis spectrophotometer (UV-1800PC, Mapada Instruments, China). The relative concentrations (C/C_0) of the dye solutions were determined by the absorbance (A/A_0) at certain wavelengths (i.e., RhB = 551 nm; MO = 464 nm; MB = 663 nm [52]), due to the relationship of $C = k'A$. Here, k' is a constant, A is the absorbance of the dye aq. solution at time t, and A_0 is the absorbance at the beginning of the visible-light irradiation. C is the concentration of the dye aqueous solution at time t, and C_0 is the concentration at the beginning of the visible-light irradiation. The photocatalytic experimental method under sunlight was similar to those under visible light irradiation.

The organic dyes (i.e., RhB, MO and MB) can absorb some visible light. To avoid the effect of visible-light absorption on the photocatalytic activity, we also carefully chose alcohols (i.e., methanol and isopropanol) without visible-light absorption in wavelength of 300–800 nm as the target substances to corroborate the photocatalytic activity of the as-obtained Ag/AgCl photocatalysts. The photodegradation of alcohols was conducted in aqueous alcohol suspensions with Ag/AgCl photocatalysts ($FR_{30}PVP_{0.05}$, 1 g L^{-1}) under the similar visible-light irradiation (λ ≥ 420 nm). Typically, for photodegradation of isopropanol, 50 mg of $FR_{30}PVP_{0.05}$ photocatalyst was firstly dispersed in 25 mL of H$_2$O under magnetic stirring for 15 min and ultrasonic treating for another 15 min;
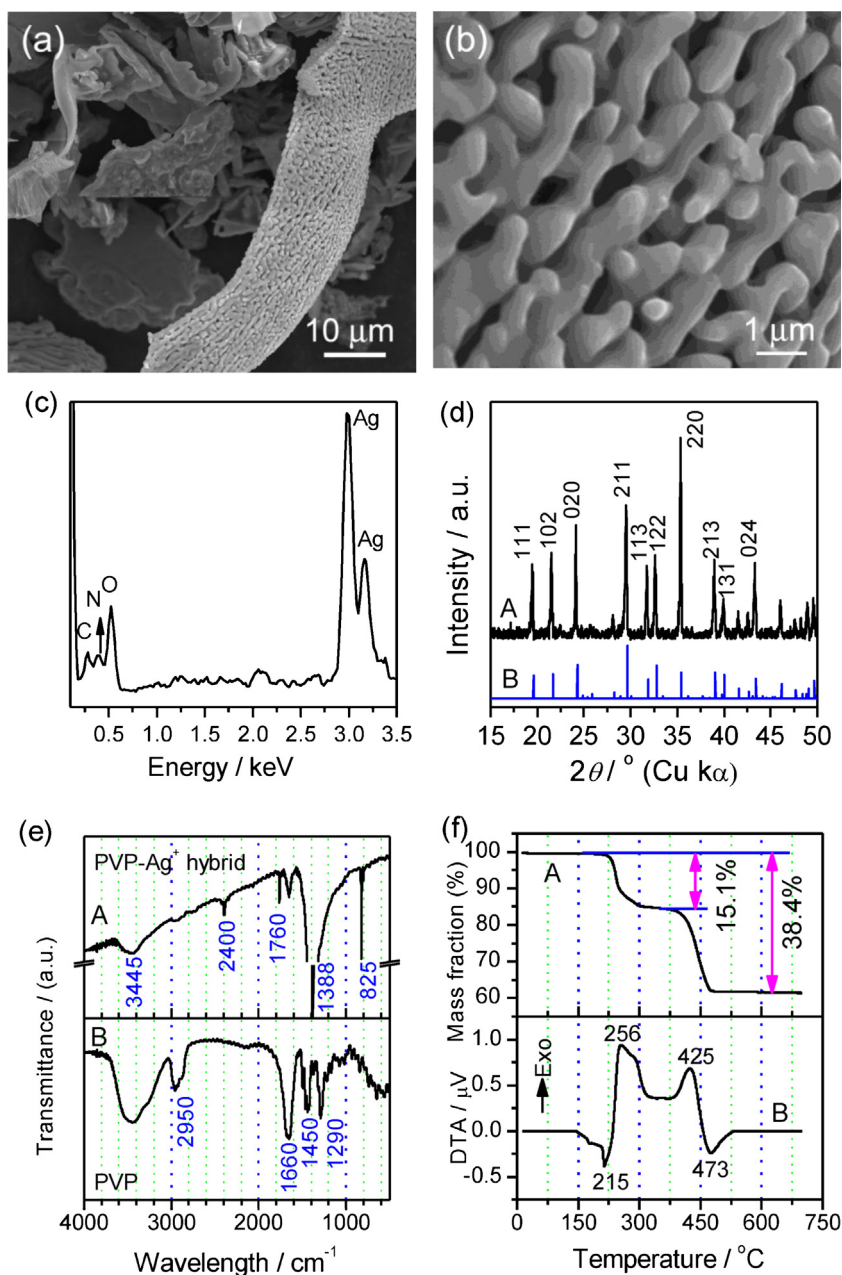
Fig. 2. (a and b) FE-SEM images, (c) EDS spectrum, (d) XRD pattern (JCPDS no. 43-0649), (e) FT-IR spectrum and (f) TG-DTA curves of the freeze-dried PVP–Ag^+ hybrid precursor with $R_{PVP/Ag} = 0.05$.

then 25 mL of isopropanol aqueous solution (~200 mg L^{-1}) was added to the above suspension under magnetic stirring. Finally, the as-obtained isopropanol aqueous solution with a final concentration of ~100 mg L^{-1} containing FR$_{30}$PVP$_{0.05}$ were irradiated with visible light (~400 mW cm^{-2}). About 10 mL of liquids was withdrawn from the above suspension after different irradiation times (i.e., 0, 15, 30, 45 and 60 min), and then the clear solutions were collected by centrifugation twice at 8000 rpm for 6 min. The experimental process for photo-degrading methanol was the same to the case of isopropanol, except that the final concentration of methanol was 200 mg L^{-1} and the irradiation intensity used was 100 mW cm^{-2}. The amounts of the residual organic substances in the solutions after various photodegradation times were determined by chemical oxygen demand (COD), measured according to the standard method of potassium dichromate titration (GB 11914-89).

3. Results and discussion

3.1. Formation and characterization of porous PVP–Ag^+ precursors

The synthesis of solid PVP–Ag^+ precursors via the freeze-drying process is the key step toward hierarchical Ag/AgCl nanocrystals (Fig. 1). The mixture of AgNO$_3$ and PVP in ethanol/water is yellow in color, which suggests that Ag^+ ions react with pyrrolidone rings of PVP molecules to form a kind of PVP–Ag^+ complex ions. After evaporation of the solvents under freeze-drying conditions, the PVP–Ag^+ complex ions are immobilized among the spaces of the networks derived from the organic chains of PVP molecules. The freeze-drying process favors the uniform dispersion of Ag^+ species in PVP chains through the interaction between Ag^+ species and (N,O) atoms in the pyrrolidone rings of PVP molecules.
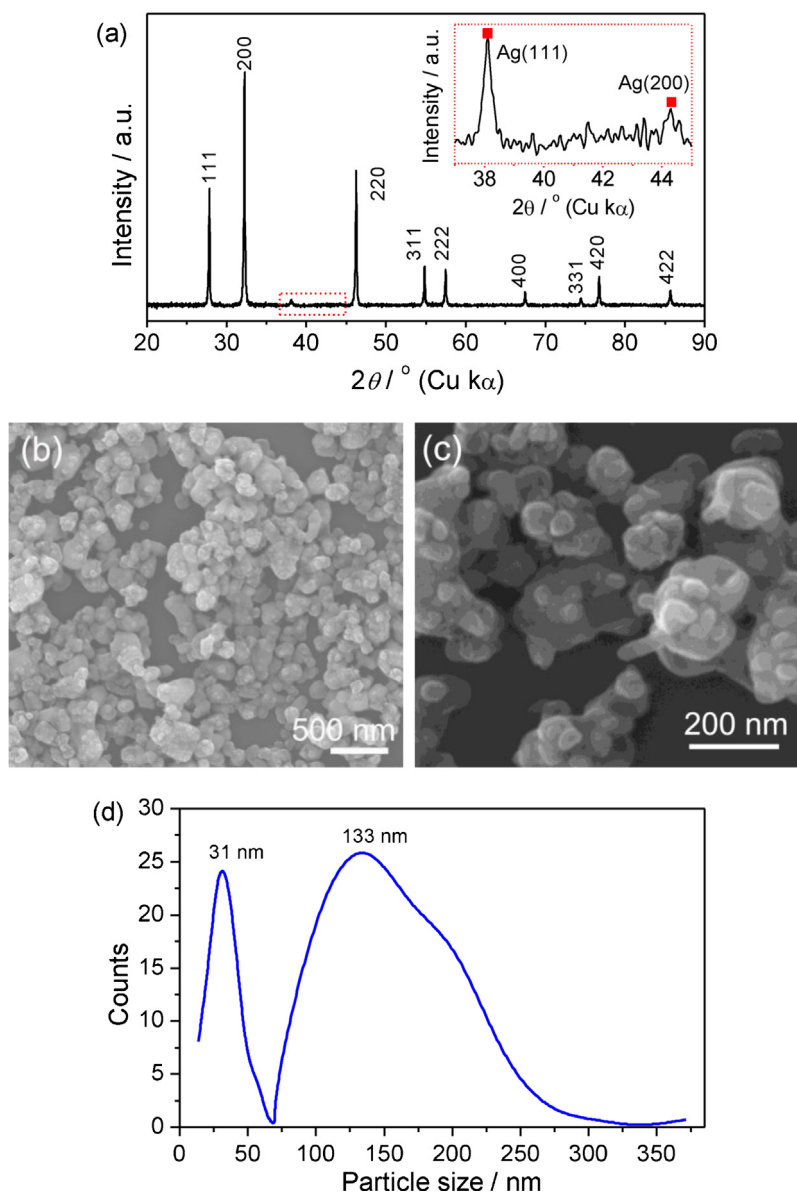
Fig. 3. (a) XRD pattern, (b and c) FE-SEM images, (d) apparent particle-size distribution histogram, and (e) its pristine particle-size-distribution histogram of the Ag/AgCl nanocrystals ($FR_{30}PVP_{0.05}$, $R_{PVP/Ag} = 0.05$, $t_r = 30$ min) obtained via the freeze-drying route.

We firstly characterized the PVP–Ag⁺ precursor ($R_{PVP/Ag} = 0.05$) obtained via the freeze-drying route, and the typical results are shown in Fig. 2. Fig. 2a and b shows the typical FE-SEM images of the PVP–Ag⁺ precursor. The sample takes on a porous plate-like morphology with an apparent size range of 10–50 μm in edge length, but the constituent units are smaller than 1 μm (Fig. 2b). The corresponding EDS spectrum in Fig. 2c indicates that the PVP–Ag⁺ precursor consists of elemental C, N, O, and Ag, belonging to PVP and AgNO₃ molecules. A typical XRD pattern of the PVP–Ag⁺ precursor in Fig. 2d indicates that the precursor is mainly composed of crystalline AgNO₃ species (JCPDS card no. 43-0649). In addition, the strongest peak in the standard data (spectrum B in Fig. 2d) is from the (2 1 1) reflection, whereas the PVP–Ag⁺ precursor shows the strongest peak from the (2 2 0) reflection. The enhancement of the (2 2 0) reflection in intensity suggests that the AgNO₃ crystals in the PVP–Ag⁺ precursor show a preferred orientation along the [2 2 0] direction, because of synergistic effect of PVP molecules and freeze-drying process.

Fig. 2e shows the FT-IR spectra of the PVP–Ag⁺ precursor and pure PVP. The wide absorption bands at ∼3445 cm⁻¹, belonging to the −OH stretching vibration and absorbed water molecules, exist both in the PVP–Ag⁺ precursor and pure PVP sample. The bands at 2850–2950 cm⁻¹ corresponds to the stretching vibration of C−H bonds in −CH₃ and −CH₂ groups of PVP molecules [73]. The bands at ∼1660 cm⁻¹ can correspond to the C=O and C−N stretching vibration of the pyrrolidone rings of PVP [73]. The bands at ∼1450 cm⁻¹ and ∼1290 m⁻¹ correspond to antisymmetric deformation vibration of −CH₃ groups and deformation of −CH₂ groups from PVP molecules [74]. When comparing spectrum A and B in Fig. 2e, one can find that the new bands at 2400, 1760, 1388 and 825 cm⁻¹ should be caused by the addition of AgNO₃ species. The absorption bands at ∼1760 cm⁻¹ and ∼825 cm⁻¹ should be ascribed to NO₃⁻ ions [75]. The very strong band at 1388 cm⁻¹ may due to interaction of Ag⁺ and N in the pyrrolidone rings. The band at 2400 cm⁻¹ is probably due to the complex of Ag⁺···⁻O=C, indicating the formation of an organic-inorganic hybrid [76,77].

Fig. 2f shows the TG–DTA curves of the PVP–Ag$^+$ precursor. There are two obvious mass losses in the TG (curve A): ~15.1% at 210–320 °C and 23.3% at 400–480 °C. The corresponding DTA curve (B) indicates that the first mass loss (~15.1%) is accompanied with an endothermic peak at around 215 °C and an obvious exothermic peak centered at 256 °C. The endothermic peak at around 215 °C should be ascribed to melting of AgNO$_3$ crystals, close to theirs melting point (212 °C). The exothermic peak at 256 °C mainly is due to the decomposing and carbonization of PVP molecules. For the second mass loss (23.3%), an exothermic peak at ~425 °C and an endothermic peak at ~470 °C occur in its corresponding DTA curve. The exothermic peak at ~425 °C can be ascribed to the oxidation of C derived from PVP, and the endothermic peak at ~473 °C should be due to the pyrolysis of AgNO$_3$ according to Eq. (1):

$$2AgNO_3 = 2Ag + 2NO_2 + O_2 \qquad (1)$$
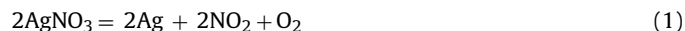
Taking the XRD, EDS, FT–IR and TG–DTA results into account, the PVP–Ag$^+$ precursor is a typical organic–inorganic hybrid substance, the composition of which can be described as $(C_6H_9NO)_x(AgNO_3)$. Supposing that the final product of the $(C_6H_9NO)_x(AgNO_3)$ precursor after treating at 600 °C is Ag, the x value can be calculated to be ~0.048 according to the total mass loss (~38.4%) in the TG curve. It is very close to the theoretic value of $R_{PVP/Ag} = 0.05$.

3.2. Formation and characterization of hierarchical Ag/AgCl nanocrystals

Hierarchical Ag/AgCl nanocrystals (FR$_{30}$PVP$_{0.05}$) were synthesized by photoreducing AgCl species, which were derived via a precipitation reaction between the solid porous PVP–Ag$^+$ precursor and Cl$^-$ aq. solution. Fig. 3a shows a typical XRD pattern of the sample obtained by photo-reducing AgCl suspension for 30 min using a Xe lamp. The major diffraction peaks can be readily indexed to the cubic AgCl phase (JCPDS card no. 31-1238). The weak peaks at 38.1° and 44.3° shown in the inlet of Fig. 3a can be attributed to the (1 1 1) and (2 0 0) reflections of cubic Ag^0 phase (JCPDS card no. 65-2871), respectively. According to Fig. 3a, the as-obtained sample is an Ag/AgCl hybrid compound, and the content of metal Ag^0 is relatively low. A typical low-magnification SEM image (Fig. 3b) of the Ag/AgCl hybrid obtained suggests that the sample takes on a spherical particulate morphology with an apparent size range of 156 ± 50 nm. The enlarged SEM image in Fig. 3c indicates that the surfaces of the large Ag/AgCl particles are covered with small Ag/AgCl nanoparticles with a size range of 33 ± 12 nm. The particle-size distribution curve of the large and small Ag/AgCl particles, derived by statistical analysis of their SEM images, is shown in Fig. 3d. One can find that there are two peaks centered at 31 nm and 133 nm, respectively. The as-obtained Ag/AgCl sample is therefore hierarchical in microstructure, and well-dispersed.

The elemental compositions and their chemical states of the hierarchical Ag/AgCl nanocrystals (FR$_{30}$PVP$_{0.05}$) were characterized using XPS spectra (Fig. 4). Fig. 4a shows the survey spectrum, which indicates that the Ag/AgCl nanoparticles obtained are mainly composed of Ag, Cl, C and O elements. Fig. 4b shows the high-resolution Ag 3d spectrum. There are two peaks at around 367.4 eV and 373.4 eV, which can be ascribed to Ag 3d$_{5/2}$ and Ag 3d$_{3/2}$, respectively [51,53,57]. The Ag 3d$_{5/2}$ and Ag 3d$_{3/2}$ peaks of Ag^0 species usually locate at 368.3 and 374.3 eV [31], and the Ag 3d$_{5/2}$ and Ag 3d$_{3/2}$ peaks of Ag$^+$ species in AgCl are reported at ~367 and 373 eV [78,79], respectively. The present Ag 3d data (367.4 eV for Ag 3d$_{5/2}$ and 373.4 eV for Ag 3d$_{3/2}$) should be the superposition of the 3d binding energy of Ag^0 and Ag$^+$ species [57]. However, the peaks in Fig. 4b are difficult to divide into two sets of peaks belonging to Ag^0 and Ag$^+$ species, respectively. This point may indicate that the Ag^0 species and AgCl particles have a special composite structure, being different from either of their individual species
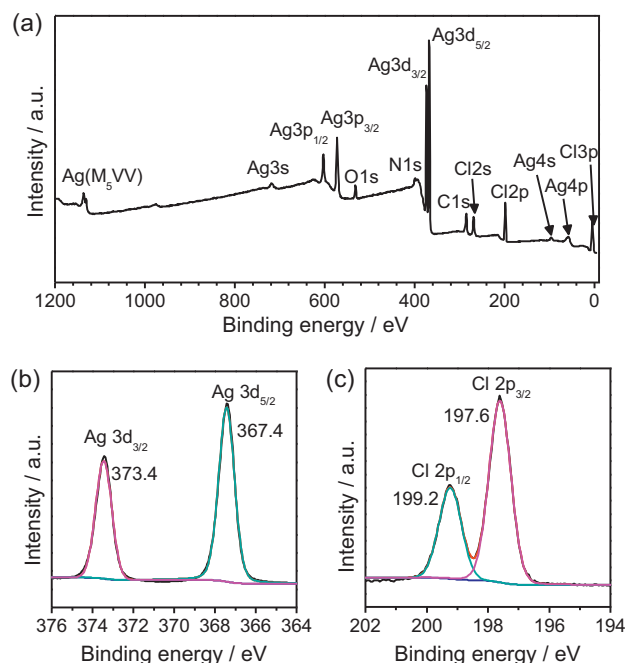

Fig. 4. Typical XPS spectra of the Ag/AgCl nanocrystals (FR$_{30}$PVP$_{0.05}$, $R_{PVP/Ag} = 0.05$, $t_r = 30$ min): (a) survey scan spectrum, (b and c) high-resolution spectra of (b) Ag 3d and (c) Cl 2p.

[53,60]. Fig. 4c shows two peaks at about 197.6 eV and 199.2 eV, which can be attributed to Cl 2p$_{3/2}$ and Cl 2p$_{1/2}$, respectively, from AgCl [57]. According to the XPS spectra, the surface atomic Ag-to-Cl ratio calculated is approximately 1.14, suggesting the existence of Ag^0 species, and the molar Ag^0-to-AgCl ratio is ~14%. In addition, the N 1s spectrum (Fig. S1a, ESI) shows two weak peaks at ~399.8 and 394.5 eV, which may be attributed to the elemental N from PVP molecules and NO$_3^-$ absorbed on the surfaces of the solid Ag/AgCl particles, respectively [46]. The O 1s XPS spectrum (Fig. S1b, ESI) shows two peaks at ~531.4 and 532.5 eV, which can be attributed to absorbed inorganic O species (e.g., NO$_3^-$) and organic O species of PVP molecules, respectively [18]. The C 1s XPS spectrum (Fig. S1c, ESI) shows three peaks at 284.6, 285.8 and 287.6 eV, respectively. The peak at 284.6 eV should be ascribed to adventitious carbon [53], and the peaks at 285.8 and 287.6 eV may be attributed to C combined with N, O and Cl atoms from the PVP species absorbed on the surfaces of the Ag/AgCl nanoparticles [80]. The survey scan and high-resolution XPS spectra of the hierarchical Ag/AgCl nanocrystals indicate that AgCl is the major component with a small amount of Ag^0 species, and the trace amount of elemental C, O and N is from PVP molecules absorbed.

3.3. Photodegradation performance of hierarchical Ag/AgCl nanocrystals derived from freeze-frying route

To evaluate the photocatalytic activity of the as-obtained Ag/AgCl nanocrystals, three organic dyes (MO, RhB and MB) were used as target substances to test their photodegradation performance under visible-light irradiation ($\lambda \geq 420$ nm, 400 mW cm^{-2}). Fig. 5 shows the typical photodegradation properties of the hierarchical Ag/AgCl nanocrystals (FR$_{30}$PVP$_{0.05}$) obtained under freeze-drying conditions with $R_{PVP/Ag} = 0.05$ and $t_r = 30$ min. The changes of the UV–vis absorption spectra of MO, RhB and MB aqueous solutions with various irradiation times in the presence of hierarchical Ag/AgCl photocatalysts are shown in Fig. 5a–c, respectively. One can find that the total fading durations of the MO, RhB and MB aqueous solutions (10 mg L^{-1}) are 2 min, 3 min and 4 min,
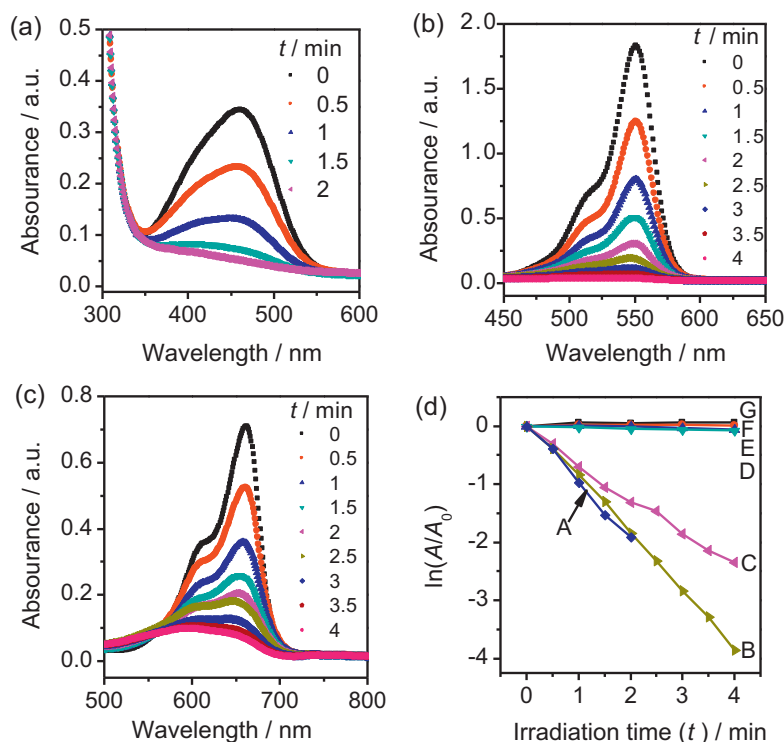
Fig. 5. Typical UV–vis spectral changes of (a) MO, (b) RhB and (c) MB aqueous solutions (50 mL, 10 mg L^{-1}) with different irradiation times in the presence of Ag/AgCl nanocrystals (FR$_{30}$PVP$_{0.05}$, $R_{PVP/Ag}$ = 0.05, t_r = 30 min, 25 mg) under visible-light irradiation (400 mW cm^{-2}, $\lambda \geq$ 420 nm); (d) plots of ln(A/A_0) versus visible-light irradiation times for different organic dyes with or without photocatalysts: (A) MO with Ag/AgCl, (B) RhB with Ag/AgCl, (C) MB with Ag/AgCl, (D) RhB with P25, and (E–G) MB, RhB and MO without any photocatalysts.

respectively, under the visible-light irradiation conditions. Fig. 5d compares the plots of ln(A/A_0) versus visible-light irradiation times for different organic dyes with or without photocatalysts. One can see that the MB, RhB and MO aq. solutions cannot be faded without any photocatalysts or with TiO$_2$ (P25) under visible-light irradiation for 4 min, as shown as curves D–G in Fig. 5d. For the cases of hierarchical Ag/AgCl photocatalysts (FR$_{30}$PVP$_{0.05}$), the ln(A/A_0) has a good linear relationship with irradiation time (t/min), and the fitting results are shown in Eqs. (2)–(4) according to the experimental data in Fig. 5d. The linearity in the ln(A/A_0)–t plots indicates that these photodegradation reactions follow the first-order kinetics, and the photodegradation rates (k/min^{-1}) can be calculated to be 0.99(4), 0.97(1) and 0.58(2) min^{-1} for MO, RhB and MO, respectively, according to their slops. The degradation rates of the hierarchical Ag/AgCl nanocrystals obtained via the freeze-drying route presented here are much higher than those of the Ag/AgCl nanocrystals synthesized by other methods [51,55–57,59].

$$\ln\left(\frac{A}{A_0}\right)_{MO} = -0.99(4)t + 0.03(5), \quad R^2 = 0.992 \tag{2}$$

$$\ln\left(\frac{A}{A_0}\right)_{RhB} = -0.97(1)t + 0.09(3), \quad R^2 = 0.998 \tag{3}$$

$$\ln\left(\frac{A}{A_0}\right)_{MB} = -0.58(2)t + 0.06(4), \quad R^2 = 0.993 \tag{4}$$

The stability and recycling performance of the hierarchical Ag/AgCl photocatalyst (FR$_{30}$PVP$_{0.05}$) obtained was also investigated using RhB aq. solutions as the target dye under visible-light irradiation. Fig. 6 shows the typical degradation curves after three cycles. One can find that the as-obtained Ag/AgCl nanocrystals show a fairly stable photocatalytic performance in recycling. The slow decrease in the 3rd cycle can be attributed to the loss of the

photocatalysts during the recycling experiments. The results indicate that the hierarchical Ag/AgCl nanocrystals obtained is active and stable as visible-light-driven photocatalysts.

Sunlight is the low-cost, clean and infinite energy to drive photocatalysts for depollution of environment. Fig. 7 shows the typical results of sunlight-driven photodegradation performance of RhB aq. solutions in the presence of the hierarchical Ag/AgCl nanocrystals (FR$_{30}$PVP$_{0.05}$) obtained from the freeze-dying route. The RhB aq. solutions can be completely photodegradated in 25 min under real sunlight with an illumination intensity of 40 $\pm$ 5 mW cm^{-2} (Fig. 7a). Fig. 7b shows the plots of A/A_0 and ln(A/A_0) versus irradiation times of sunlight. The photodegradation rate can be calculated to be 0.158(7) min^{-1} according to the linear fitting (R^2 = 0.99) of the ln(A/A_0)–t plot.
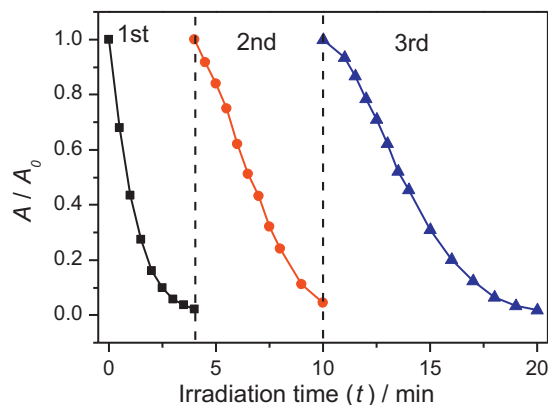
Fig. 6. Cycling degradation curves of the Ag/AgCl nanocrystals (FR$_{30}$PVP$_{0.05}$, $R_{PVP/Ag}$ = 0.05, t_r = 30 min) for RhB aq. solutions (400 mW cm^{-2}, $\lambda \geq$ 420 nm).
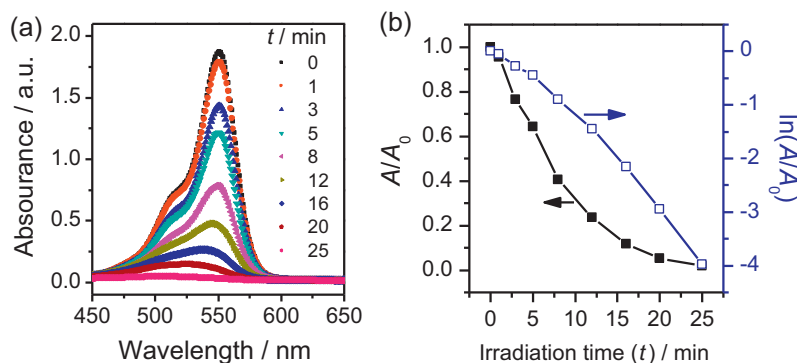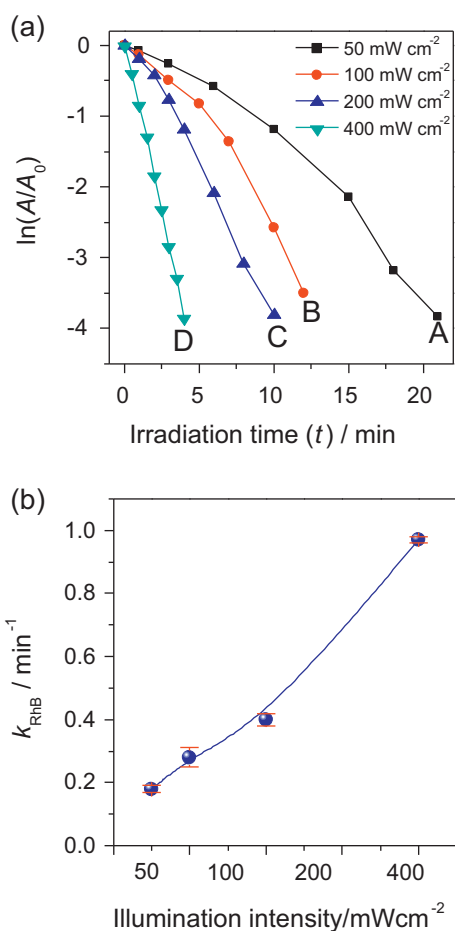
Fig. 7. (a) Typical UV–vis spectral changes of RhB aq. solutions (50 mL, 10 mg L^{-1}) in the presence of the Ag/AgCl nanocrystals ($R_{PVP/Ag}$ = 0.05, t_r = 30 min, 25 mg) under sunlight irradiation (40 ± 5 mW cm^{-2}) with various irradiation times; (b) the corresponding Plot of A/A_0 versus irradiation time.

The illumination intensities of the visible light used for the photodegradation of organic dyes have a key effect on the degradation rates. Fig. 8 shows the illumination-intensity-dependent performance of the as-obtained hierarchical Ag/AgCl nanocrystals (FR$_{30}$PVP$_{0.05}$) in photodegradating RhB aq. solutions under visible-light irradiation ($\lambda \geq 420$ nm) with various illumination intensities of 50–400 mW cm^{-2}. One can find that the times needed for completely degradating the similar RhB aq. solutions increase from 3 min to 20 min as the illumination intensity decreases from 400 mW cm^{-2} to 50 mW cm^{-2}, as shown in Fig. 8a. The plot of the degradation rate (k_{RhB}/min^{-1}) versus the illumination intensity of the visible light used in the photodegradation experiments is shown in Fig. 8b. One can find that the degradation rate is roughly positive proportional to the illumination intensity, and the RhB degradation rate increases from 0.18(1) to 0.97(1) min^{-1} when the illumination intensity increases from 50 to 400 mW cm^{-2}.
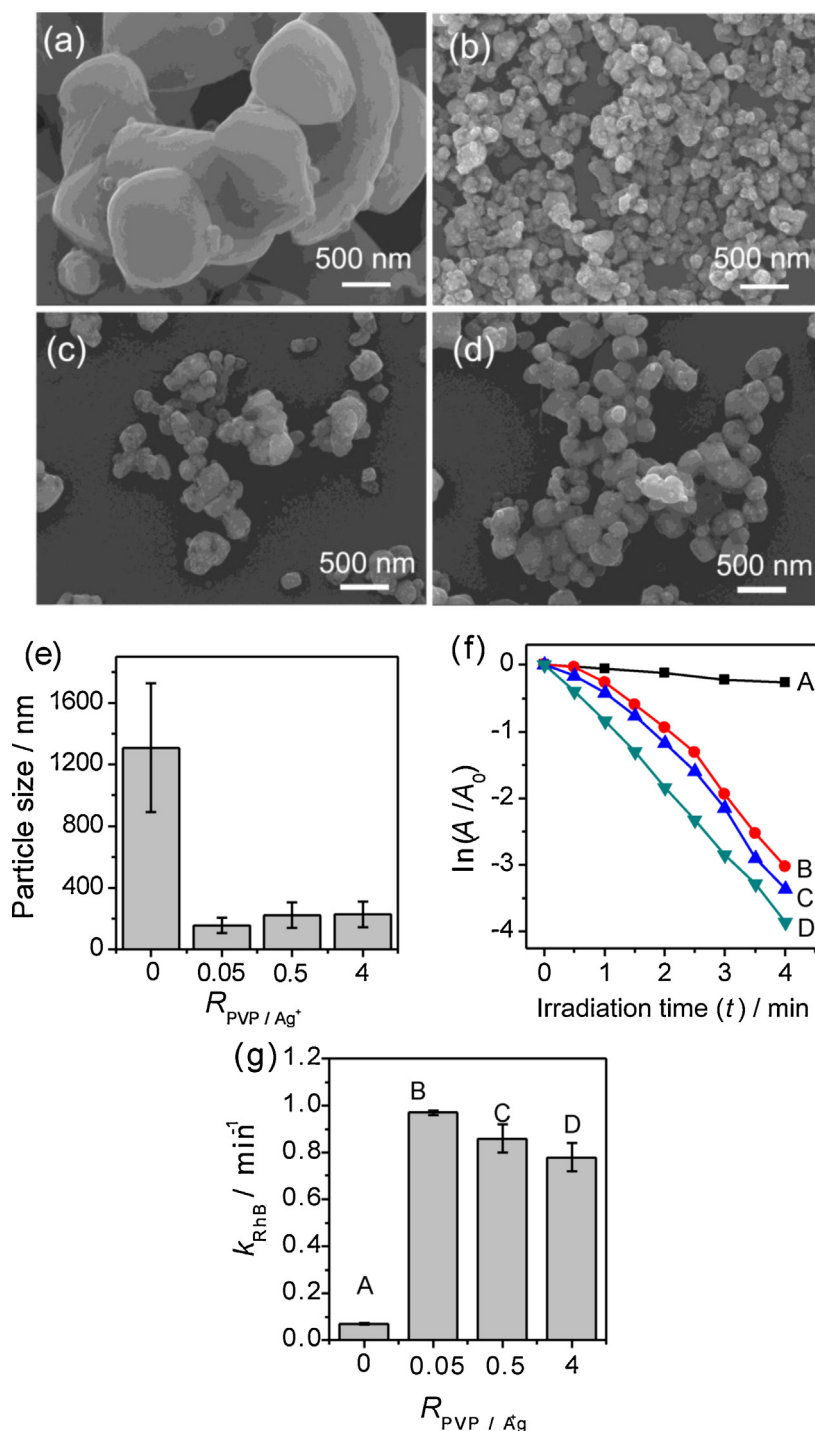
3.4. Effects of processing parameters on performance of Ag/AgCl photocatalysts

To understand the effect of PVP molecules on formation of Ag/AgCl nanocrystals, we synthesized a series of Ag/AgCl samples using the similar freeze-dying route, but with different amounts of PVP. Figs. 9a–d show the Ag/AgCl samples synthesized with various molar ratios ($R_{PVP/Ag}$) of the repetitive units of PVP to Ag$^+$ species: $R_{PVP/Ag}$ = 0 (FR$_{30}$PVP$_0$, Fig. 9a), $R_{PVP/Ag}$ = 0.05 (FR$_{30}$PVP$_{0.05}$, Fig. 9b), $R_{PVP/Ag}$ = 0.5 (FR$_{30}$PVP$_{0.5}$, Fig. 9c) and $R_{PVP/Ag}$ = 4 (FR$_{30}$PVP$_4$, Fig. 9d). One can find that the Ag/AgCl sample synthesized without PVP takes on an agglomerated particulate morphology with a size range of 1.3 ± 0.4 μm, whereas the ones synthesized with PVP are well-dispersed nanoparticles with remarkably decreased particle sizes (less than 300 nm). Fig. 9e gives the statistical particle-size histogram of the Ag/AgCl samples synthesized with various amounts of PVP. The addition of PVP molecules is favorable in forming Ag/AgCl nanocrystals with small particle sizes (150–230 nm), but excess PVP species have adverse effects in decreasing their particle sizes. When the $R_{PVP/Ag}$ is 0.05, the apparent particle size of the Ag/AgCl nanocrystals is smaller than that of the Ag/AgCl samples with $R_{PVP/Ag}$ of 0.5 or 4. A moderate amount of PVP can control the growth of AgCl particles because of the steric effect of the apolar PVP chains, whereas excess apolar chains of the PVP molecules are easy to form capsules, which is harmful in controlled growth of nanocrystals.

The photodegradation performance of the Ag/AgCl samples synthesized with various $R_{PVP/Ag}$ values is shown in Fig. 9f, and their corresponding degradation rates is shown in Fig. 9g. One can find that the FR$_{30}$PVP$_{0.05}$ sample with $R_{PVP/Ag}$ = 0.05 has the highest degradation rate (k = 0.97(1) min^{-1}) among these samples, and the FR$_{30}$PVP$_0$ sample without PVP has the lowest rate (k = 0.069(5) min^{-1}). When taking the SEM images, particle sizes and microstructures into account, the enhanced photocatalytic performance of the Ag/AgCl nanocrystals ($R_{PVP/Ag}$ = 0.05) is mainly due to their decreased particle sizes and hierarchical microstructures (Fig. S2, ESI).

The photoreduction times (t_r) used during the course of the synthesis of Ag/AgCl photocatalysts have, to a certain extent, a direct proportion to the amounts of metal Ag^0 species, which

Fig. 8. (a) Typical plots of ln(A/A_0) of RhB aq. solutions (50 mL, 10 mg L^{-1}) versus irradiation times in the presence of Ag/AgCl nanocrystals ($R_{PVP/Ag}$ = 0.05, t_r = 30 min, 25 mg) under visible-light irradiation ($\lambda \geq 420$ nm) with various illumination intensities of (A) 50 mW cm^{-2}, (B) 100 mW cm^{-2}, (C) 200 mW cm^{-2}, and (D) 400 mW cm^{-2}; (b) a relationship curve of the RhB degradation rates versus the intensity of visible-light irradiation in the presence of Ag/AgCl nanocrystals.

Fig. 9. (a–d) Typical FE-SEM images of Ag/AgCl nanocrystals prepared via the freeze-drying route with various molar PVP-to-Ag⁺ ratios ($t_r = 30$ min): (a) $R_{PVP/Ag} = 0$, (b) $R_{PVP/Ag} = 0.05$; (c) $R_{PVP/Ag} = 0.5$ and (d) $R_{PVP/Ag} = 4$; (e) apparent particle-size distribution of the samples prepared with various molar PVP-to-Ag⁺ ratios; (f) plots of $\ln(A/A_0)$ vs. irradiation time in the presence of Ag/AgCl nanocrystals obtained with various molar PVP-to-Ag⁺ ratios for RhB degradation under the same visible-light conditions ($\lambda \geq 420$ nm, 400 mW cm⁻²); (g) comparison of the RhB degradation rates of the Ag/AgCl nanocrystals obtained with various PVP-to-Ag⁺ ratios.

are expected to influence the photocatalytic performance of the plasmonic Ag/AgCl photocatalysts. Fig. 10 shows the typical photocatalytic performance of the Ag/AgCl photocatalysts ($R_{PVP/Ag} = 0.05$) synthesized by exposing the AgCl suspensions to a Xe lamp for various reduction times ($t_r = 0, 5, 10, 30$ and 60 min) under ambient conditions. Fig. 10a shows the $\ln(A/A_0)$–t plots of RhB aq. solutions in the presence of the above-mentioned Ag/AgCl photocatalysts synthesized with various photoreduction times. Fig. 10b shows the comparison of their photodegradation rates (k/min⁻¹) calculated

according to the slopes of the linear fitting curves of the $\ln(A/A_0)$–t plots shown in Fig. 10a. One can find that the photodegradation rates of the Ag/AgCl samples rapidly increase from 0.51(5) to 1.04(4) min⁻¹ with the increase in photoreduction time from 0 to 10 min, but further time expand in photoreduction does not have a positive effect in the enhancement of photodegradation performance. The optimum photoreduction time can be 10–30 min under a Xe lamp (400 mW cm⁻²), because of the highest photodegradation rate (Fig. 10b). The above results also suggest that not only the

(a)

(b)
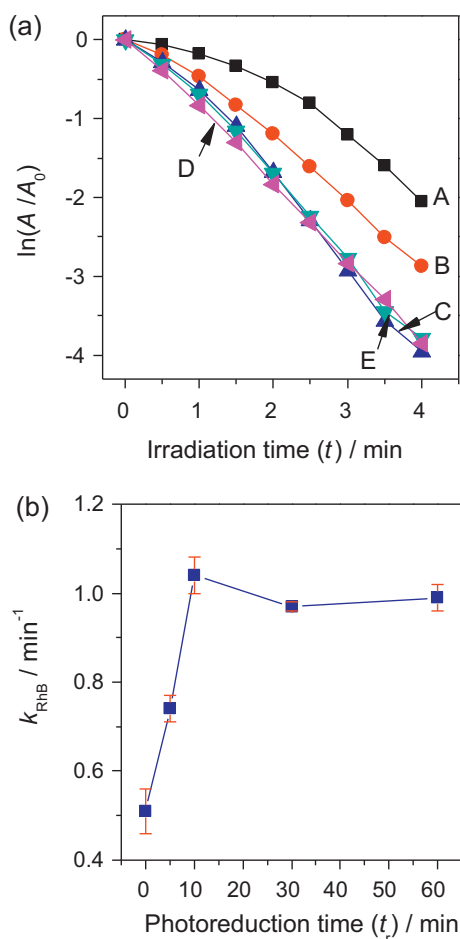
Fig. 10. (a) Plots of $\ln(A/A_0)$ of RhB aq. solutions versus the irradiation time under visible light ($\lambda \geq 420$ nm, 400 mW cm^{-2}) in the presence of Ag/AgCl nanocrystals prepared with various photo-reduction times ($R_{PVP/Ag} = 0.05$): (A) $t_r = 0$ min, (B) $t_r = 5$ min, (C) $t_r = 10$ min, (D) $t_r = 30$ min, and (E) $t_r = 60$ min; (b) comparison of the RhB degradation rates of the Ag/AgCl nanocrystals obtained with various photo-reduction times under visible-light irradiation ($\lambda \geq 420$ nm, 400 mW cm^{-2}).

microstructures of the Ag/AgCl nanocrystals, but also their amounts of metal Ag species influence the photocatalytic performance of the Ag/AgCl photocatalysts in decomposing organic dyes under visible-light irradiation.

To further demonstrate the effects of PVP molecules and the freeze-drying process on the morphology and microstructure, we comparatively synthesized Ag/AgCl samples with various shape-control agents (e.g., PEG), using (or not using) the freeze-drying process. Fig. 11 shows the typical results. Fig. 11a shows the SEM image of the Ag/AgCl sample (FR$_{30}$PEG$_{0.05}$) synthesized with PEG via the similar freeze-drying process. It consist of large spherical particles with smooth surfaces, and their particle-size range is 800–1400 nm, as shown in Fig. 11c. The size and morphology of the FR$_{30}$PEG$_{0.05}$ sample obtained with PEG are distinctly different from those of the Ag/AgCl sample (FR$_{30}$PVP$_{0.05}$), which consists of small, hierarchical and well-dispersed nanoparticles (Fig. 3). Fig. 11b shows a typical SEM image of the Ag/AgCl sample (PR$_{30}$PVP$_{0.05}$) synthesized with PVP but no using freeze-drying process, and its particle-size distribution is shown in Fig. 11c. One can find that the sizes and shapes of the primary particles in the PR$_{30}$PVP$_{0.05}$ sample are similar to those of the Ag/AgCl sample (FR$_{30}$PVP$_{0.05}$) obtained with freeze-drying process, but the agglomeration phenomenon of the PR$_{30}$PVP$_{0.05}$ sample is much more serious than that of the FR$_{30}$PVP$_{0.05}$ sample. When taking Figs. 3b–e, 9a–e and 11a–c into account, we can conclude that PVP molecules is favorable in

forming small and hierarchical Ag/AgCl nanostructures, whereas the freeze-drying process during the preparation of PVP–Ag$^+$ hybrid precursors is helpful to achieve well-dispersed Ag/AgCl nanocrystals.

Fig. 11d compares the visible-light-driven photodegradation performance of RhB aq. solutions in the presence of the Ag/AgCl samples obtained various conditions. The Ag/AgCl sample (FR$_{30}$PEG$_{0.05}$) with PEG shows the lowest degradation rate ($k = 0.077(8)$ min^{-1}), and the degradation rate ($k = 0.51(1)$ min^{-1}) of the PR$_{30}$PVP$_{0.05}$ sample without freeze-drying treatment is lower than that ($k = 0.97(1)$ min^{-1}) of the Ag/AgCl sample (FR$_{30}$PVP$_{0.05}$). The enhanced photocatalytic performance of the freeze-dried Ag/AgCl sample with PVP should be attributed to their small sizes, good dispersibility and hierarchical microstructures, which provide higher specific areas and more photocatalytic active spots.

### 3.5. Mechanism understanding for the synthesis of Ag/AgCl photocatalysts and their photocatalytic performance

To understand the formation mechanism of the hierarchical Ag/AgCl nanocrystals, we investigated the growth process and morphological evolution of the AgCl nanocrystals derived by precipitating the freeze-dried PVP–Ag$^+$ hybrid precursors with a Cl$^-$ aq. solution. Fig. 12 shows the typical SEM images of the AgCl nanocrystals derived by magnetically stirring the suspensions from the precipitated products of the porous PVP–Ag$^+$ hybrid precursor ($R_{PVP/Ag} = 0.05$) with a Cl$^-$ aq. solution under a dark condition for 5–120 min. One can find that the apparent particle sizes and morphologies of the samples with various stirring times in dark are similar, indicating that the growth of AgCl nanocrystals was finished in the initial several minutes. In addition, when comparing Fig. 12a–c, one can conclude that the small AgCl particles (20–30 nm) attached on the surfaces of the large ones should grow during the course of magnetic stirring in dark, and therefore the small particles of the samples with photoreduction shown in Fig. 3b and c are also AgCl species. The Ag^0 species in situ formed in AgCl particles during the course of photoreduction may be embed in the AgCl matrix in a highly dispersed manner.

The PVP-assisted freeze-drying route developed in the present work is efficient in controlled synthesis of hierarchical Ag/AgCl nanocrystals with small sizes. The formation mechanism can be understood as followings. Firstly, Ag$^+$ and PVP chains form a Ag$^+$–PVP complex in liquid solutions, and the Ag$^+$ ions uniformly disperse in the voids of PVP chains. Secondly, the rapid freeze treatment is helpful to immobilize Ag$^+$ ions in the chains of PVP molecules uniformly due to complexing reaction between Ag$^+$ ions with the N,O atoms of the pyrrollidone rings, and the followed vacuum frying process transforms the freezed Ag$^+$–PVP complex to a solid and porous Ag$^+$–PVP precursor. Fourthly, when the porous Ag$^+$–PVP precursor solids react with Cl$^-$ aq. solutions, hierarchical AgCl nanoparticles are rapidly in situ formed in the voids of PVP chains. Finally, the hierarchical Ag/AgCl nanocrystals are formed by photoreducing AgCl nanoparticles to in situ grow small amounts of Ag^0 species in AgCl particles. The solid, porous Ag$^+$–PVP precursors play a key role in the controlled synthesis of the hierarchical Ag/AgCl nanocrystals with small particle sizes.

Photocatalytic performance driven by visible light is usually dependent on the optical absorption property of a photocatalyst. Fig. 13a shows the typical UV–vis diffuse reflectance spectra of AgCl and Ag/AgCl samples synthesized under different conditions. The hierarchical Ag/AgCl nanocrystals (FR$_{30}$PVP$_{0.05}$, $R_{PVP/Ag} = 0.05$ and $t_r = 30$ min) synthesized via the freeze-drying route shows a wide absorption band in the range of 350–800 nm with two peaks at $\sim$390 nm and $\sim$510 nm, as shown as spectrum A in Fig. 13a. However, the AgCl nanocrystals (FR$_0$PVP$_{0.05}$, $R_{PVP/Ag} = 0.05$ and $t_r = 0$ min) obtained via the same method just without
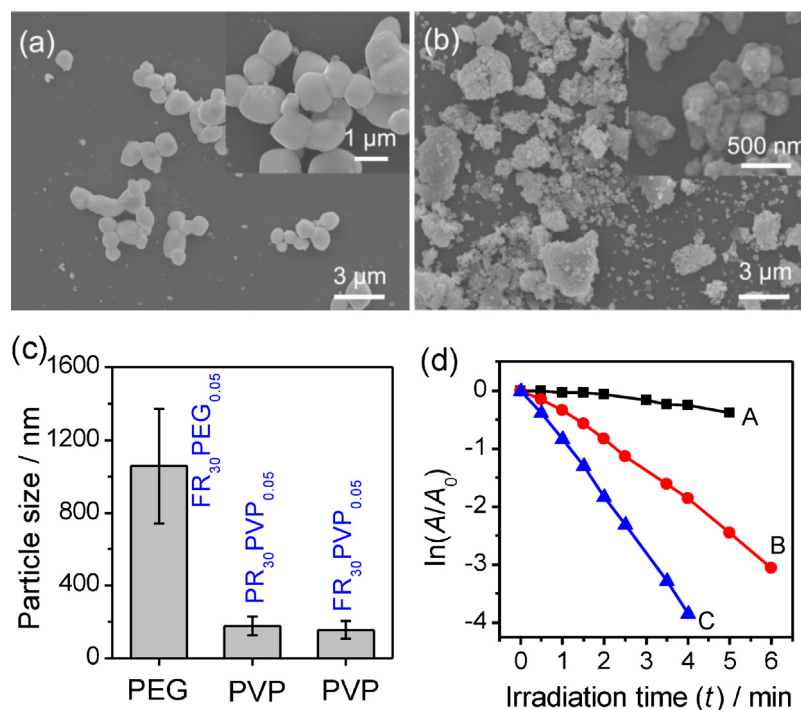
Fig. 11. (a and b) FE-SEM images of Ag/AgCl nanocrystals prepared under different conditions: (a) freeze-drying route with PEG ($R_{PEG/Ag}$ = 0.05, t_r = 30 min), and (b) direct precipitation route with PVP ($R_{PVP/Ag}$ = 0.05, t_r = 30 min); (c) the effects of additives (PVP or PEG) and processing methods (direct precipitation or freeze-drying) on the particle sizes of the Ag/AgCl nanocrystals; (d) comparative plots of ln(A/A_0) versus irradiation time in the presence of different Ag/AgCl nanocrystals (t_r = 30 min) for RhB photodegradation ($\lambda \geq$ 420 nm, 400 mW cm^{-2}): (A) freeze-dried sample with PEG ($R_{PEG/Ag}$ = 0.05), (B) directly precipitated sample ($R_{PVP/Ag}$ = 0.05), and (C) freeze-dried sample with PVP ($R_{PVP/Ag}$ = 0.05).
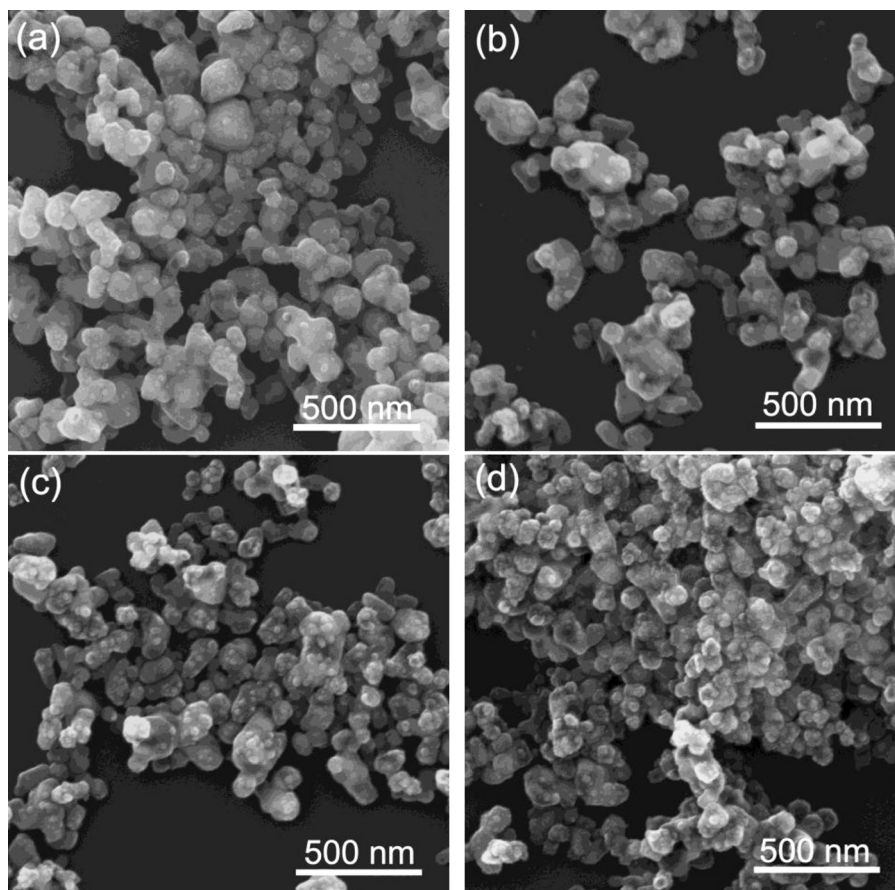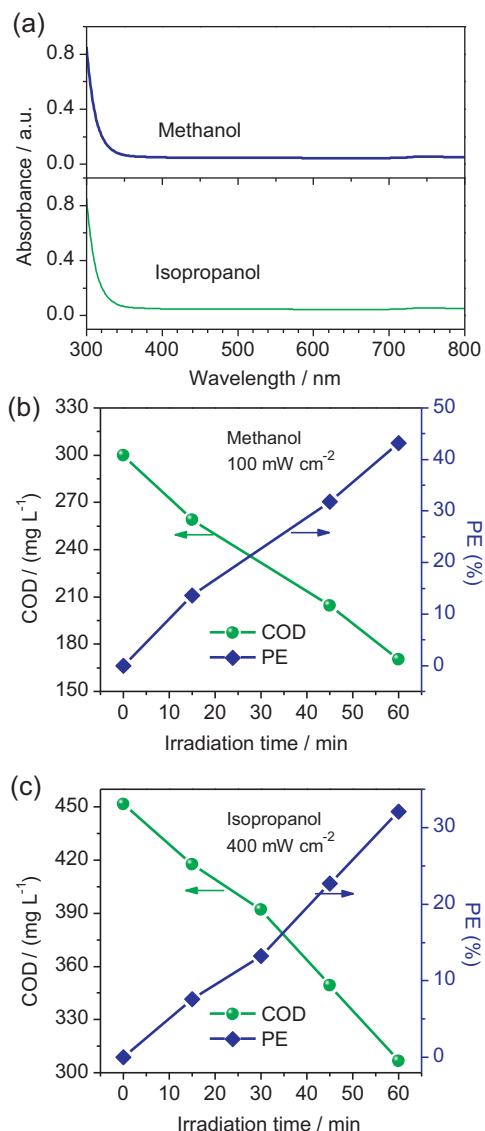

Fig. 12. Typical SEM images of AgCl nanocrystals derived by magnetically stirring the precipitated products of the porous PVP–Ag$^+$ hybrid precursor ($R_{PVP/Ag}$ = 0.05) with Cl$^-$ aq. solution under a dark condition for different stirring times: (a) 5 min, (b) 30 min, (c) 60 min and (d) 120 min.
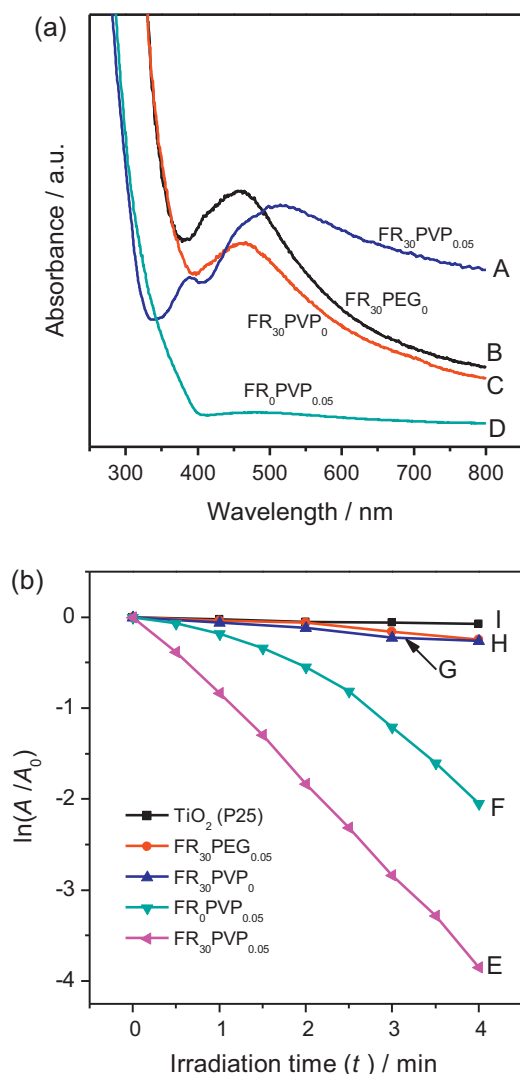
Fig. 13. (a) Typical UV–vis diffuse reflectance spectra of Ag/AgCl nanocrystals obtained at different conditions: (A) freeze-dried sample with PVP ($R_{PVP/Ag}$ = 0.05, t_r = 30 min), (B) freeze-dried sample with PEG ($R_{PEG/Ag}$ = 0.05, t_r = 30 min), (C) freeze-dried sample without PVP or PEG (t_r = 30 min), and (D) freeze-dried sample with PVP ($R_{PVP/Ag}$ = 0.05, t_r = 0 min); (b) comparison of the ln(A/A_0)–t plots for RhB photodegradation under visible-light irradiation in the presence of Ag/AgCl nanocrystals (E, F, H), AgCl (G) and TiO$_2$ (P25, I).

Fig. 14. (a) UV–vis spectra of methanol and isopropanol aqueous solutions; (b and c) photocatalytic degradation of methanol (b) and isopropanol (c) with the Ag/AgCl nanocrystals (FR$_{30}$PVP$_{0.05}$, $R_{PVP/Ag}$ = 0.05, t_r = 30 min) under visible light irradiation (λ = 3420 nm) by COD (mg L^{-1}) and photodegradation efficiency (PE %).

photoreduction show no absorption in the range of 400–800 nm, as shown as spectrum D in Fig. 13a. The wide and strong absorption bands in 350–800 nm is due to the surface plasmon resonance (SPR) effect of metal Ag species in situ grown in the AgCl particles during the photoreduction [57]. The two absorption peaks may be due to the hierarchical microstructure of the FR$_{30}$PVP$_{0.05}$ sample (Fig. 3). The Ag/AgCl sample obtained with PEG (FR$_{30}$PEG$_{0.05}$) and the one obtained without PVP (FR$_{30}$PVP$_0$) have absorption bands at ∼460 nm, as shown as spectrum B and C, respectively. The difference in UV–vis spectra of the Ag/AgCl samples is probably due to the difference in particle sizes and microstructures of metal Ag^0 species embedded among the AgCl host particles. The Ag/AgCl sample obtained with PEG consists of spherical particles with a large size of 1057 ± 315 nm (Fig. 11a), which is similar to that of the Ag/AgCl sample obtained without PVP (spherical particles, 1310 ± 420 nm, Fig. 9a), whereas the Ag/AgCl sample obtained with $R_{PVP/Ag}$ = 0.05 consists of smaller nanocrystals with a hierarchical structure (156 ± 50 nm, 33 ± 12 nm Fig. 3d). This result indicates that hierarchical Ag/AgCl nanostructures with small sizes are

favorable in efficient utilization of visible light through the wavelength range of 400–800 nm.

Fig. 13b compares the visible-light-driven photocatalytic performance of the AgCl, TiO$_2$ (P25) and Ag/AgCl samples obtained under different conditions using RhB aq. solutions as the model substance. One can find that the Ag/AgCl samples obtained without PVP (or with PEG) have low rates (k_G = 0.069(5) min^{-1}, k_H = 0.061(9) min^{-1}, plots G and H in Fig. 13b), but slightly higher than that (k_I = 0.018(2) min^{-1}) of TiO$_2$ (plot I in Fig. 13b). The low photodegradation rates are due to the large sizes ($\geq$1 μm) of the Ag/AgCl samples, although they can absorb some visible light (B, C in Fig. 13a). As plot F in Fig. 13b shown, the AgCl sample obtained via the freeze-drying route with PVP also has a relatively high rate, but its corresponding ln(A/A_0)–t plot is not linear and can be divided into several stages. The degradation rate (0.17(3) min^{-1}) at the initial stage is much lower than that (0.81(2) min^{-1}) at the late stage, which is close to the degradation rate (0.97(1) min^{-1}) of the hierarchical Ag/AgCl nanocrystals (plot E in Fig. 13b). The AgCl nanocrystals (FR$_0$PVP$_{0.05}$) have hierarchical structures with small sizes (Fig. 12c), similar to the photo-reduced Ag/AgCl product

(FR$_{30}$PVP$_{0.05}$, Fig. 3b). Visible-light irradiation during the photodegradation experiment at the initial stage can induce to form some Ag^0 species, which then accelerate the photodegradation at the late stages. When associating Fig. 13a with Fig. 13b, one can conclude that metal Ag^0 species can enhance visible-light absorbance, and the hierarchical nanostructures with small sizes can distinctly enhance the photodegradation performance.

Organic dyes have widely been used as the target substances to evaluate the activity of a photocatalyst, because their amount in a solution can be conveniently determined by a UV–vis spectrophotometer [82–84]. However, some reports have indicated that organic dyes are not suitable as probe substances to evaluate the photocatalytic activity especially under visible-light irradiation, due to their absorption in the visible-light range [85,86]. To avoid the interference of visible-light absorption of organic dyes, we choose colorless isopropanol and methanol, without absorption in visible light (Fig. 14a), as the probe substances to corroborate the photocatalytic activity of the Ag/AgCl photocatalysts (FR$_{30}$PVP$_{0.05}$) under the visible-light irradiation. The amounts of residual isopropanol and methanol in the solutions after various photocatalytic reaction times can be expressed as chemical oxygen demand (COD) [82,84]. In most cases, the COD removal usually agrees with the discoloration of the dyes solutions [87]. The photodegradation efficiency (%) can be calculated as $100 \times (COD_{initial} - COD_{final})/COD_{initial}$ [82].

Fig. 14b shows the photodegradation of methanol under visible-light irradiation of $100 \, mW \, cm^{-2}$ in the presence of Ag/AgCl (FR$_{30}$PVP$_{0.05}$) photocatalyst. One can find that the COD decreases from $300 \, mg \, L^{-1}$ to $170 \, mg \, L^{-1}$ after a photodegradation reaction of 60 min, and the photodegradation efficiency (PE) reaches ∼45%. Fig. 14c shows the photodegradation of isopropanol under the similar conditions. It also indicates an obvious decrease in COD values during the visible-light irradiation, and its photodegradation efficiency reaches ∼33% in 60 min. The above results corroborates that the Ag/AgCl nanocrystals synthesized via the present freeze-drying process have highly photocatalytic activity in degradating both organic dyes and alcohols under the condition of visible-light irradiation.

4. Conclusions

In summary, we have developed a novel and simple freeze-drying route to synthesize porous PVP–Ag$^+$ hybrid compounds, which were then efficiently transformed to hierarchical AgCl nanocrystals through a liquid-solid precipitation reaction. The AgCl nanocrystals were then conformally transformed to hierarchical Ag/AgCl nanocrystals by a partially photoreduction process. The hierarchical Ag/AgCl nanocrystals have an apparent size range of $156 \pm 50 \, nm$, and the surfaces of the large particles are covered with Ag/AgCl nanocrystals with small sizes of $33 \pm 12 \, nm$. The PVP molecules and the freeze-drying treatment have a key role in the formation of well-dispersed and hierarchical Ag/AgCl nanocrystals. The hierarchical Ag/AgCl nanocrystals obtained can be used as efficient visible-light-driven photocatalysts for decomposition of organic dyes and alcohols. The photodegradation rates were dependent on the illumination intensity of the radiation used in photocatalytic test. The RhB photodegradation rate of the hierarchical Ag/AgCl nanocrystals obtained here is ∼54 times higher than that of TiO$_2$ (P25) nanocrystals under the same test conditions. The photodegradation efficiency of methanol reaches 45% under visible-light irradiation for 60 min according to the COD values. The enhancement in visible-light-driven photodegradation performance was attributed to the SPR effect of metal Ag species embedded in the hierarchical AgCl host nanocrystals. The novelty of this work is the development of the freeze-drying process to synthesize solid and porous PVP–Ag$^+$ precursors, which are critical in the controlled formation of hierarchical AgCl and Ag/AgCl nanocrystals. The simple but robust route presented here on the basis of freeze-drying process can be expanded to synthesize other hierarchical nanostructures.

Acknowledgments

Appendix A. Supplementary data

Supplementary data associated with this article can be found, in the online version, at http://dx.doi.org/10.1016/j.apcatb.2013.07.042.

References

[1] A. Kubacka, M. Fernández-García, G. Colón, Chemical Reviews 112 (2011) 1555.
[2] Y.-G. Guo, J.-S. Hu, L.-J. Wan, Advanced Materials 20 (2008) 2878.
[3] A.L.M. Reddy, S.R. Gowda, M.M. Shaijumon, P.M. Ajayan, Advanced Materials 24 (2012) 5045.
[4] Z.L. Wang, W. Wu, Angewandte Chemie International Edition 51 (2012) 11700.
[5] X. Chen, S.S. Mao, Chemical Reviews 107 (2007) 2891.
[6] A. Fujishima, K. Honda, Nature 238 (1972) 37.
[7] M.R. Hoffmann, S.T. Martin, W. Choi, D.W. Bahnemann, Chemical Reviews 95 (1995) 69.
[8] J. Yang, D. Wang, H. Han, C. Li, Accounts of Chemical Research (2013), http://dx.doi.org/10.1021/ar300227e.
[9] N. Serpone, A.V. Emeline, The Journal of Physical Chemistry Letters 3 (2012) 673.
[10] R. Asahi, T. Morikawa, T. Ohwaki, K. Aoki, Y. Taga, Science 293 (2001) 269.
[11] J.C. Yu, H. Yu, Z. Jiang, Chemistry of Materials 14 (2002) 3808.
[12] W. Zeng, T. Liu, Z. Wang, Journal of Materials Chemistry 22 (2012) 3544.
[13] Z. Wu, G. Zhao, Y.-n. Zhang, H. Tian, D. Li, The Journal of Physical Chemistry C 116 (2012) 12829.
[14] S.E. Stanca, R. Muller, M. Urban, A. Csaki, F. Froehlich, C. Krafft, J. Popp, W. Fritzsche, Catalysis Science & Technology 2 (2012) 1472.
[15] J. Choi, H. Park, M.R. Hoffmann, The Journal of Physical Chemistry C 114 (2009) 783.
[16] H. Hao, J. Zhang, Microporous and Mesoporous Materials 121 (2009) 52.
[17] R. Abe, K. Sayama, H. Arakawa, Chemical Physics Letters 362 (2002) 441.
[18] Y. Duan, N. Fu, Q. Liu, Y. Fang, X. Zhou, J. Zhang, Y. Lin, The Journal of Physical Chemistry C 116 (2012) 8888.
[19] H. Matsumoto, T. Matsunaga, T. Sakata, H. Mori, H. Yoneyama, Langmuir 11 (1995) 4283.
[20] N. Zhang, S. Liu, Y.-J. Xu, Nanoscale 4 (2012) 2227.
[21] P. Wang, B. Huang, Y. Dai, M.-H. Whangbo, Physical Chemistry Chemical Physics 14 (2012) 9813.
[22] Y. Zhai, L. Han, P. Wang, G. Li, W. Ren, L. Liu, E. Wang, S. Dong, ACS Nano 5 (2011) 8562.
[23] I. Thomann, B.A. Pinaud, Z. Chen, B.M. Clemens, T.F. Jaramillo, M.L. Brongersma, Nano Letters 11 (2011) 3440.
[24] Y. Qu, R. Cheng, Q. Su, X. Duan, Journal of the American Chemical Society 133 (2011) 16730.
[25] D.B. Ingram, S. Linic, Journal of the American Chemical Society 133 (2011) 5202.
[26] H. Wang, T. You, W. Shi, J. Li, L. Guo, The Journal of Physical Chemistry C 116 (2012) 6490.
[27] K. Kimura, S.-i. Naya, Y. Jin-nouchi, H. Tada, The Journal of Physical Chemistry C 116 (2012) 7111.
[28] A. Kubacka, M. Ferrer, M. Fernández-García, C. Serrano, M.L. Cerrada, M. Fernández-García, Applied Catalysis B: Environmental 104 (2011) 346.
[29] Z.W. Seh, S. Liu, M. Low, S.-Y. Zhang, Z. Liu, A. Mlayah, M.-Y. Han, Advanced Materials 24 (2012) 2310.
[30] O. Rosseler, M.V. Shankar, M.K.-L. Du, L. Schmidlin, N. Keller, V. Keller, Journal of Catalysis 269 (2010) 179.
[31] J. Du, J. Zhang, Z. Liu, B. Han, T. Jiang, Y. Huang, Langmuir 22 (2006) 1307.
[32] T. Wu, S. Liu, Y. Luo, W. Lu, L. Wang, X. Sun, Nanoscale 3 (2011) 2142.
[33] C. An, S. Peng, Y. Sun, Advanced Materials 22 (2010) 2570.
[34] Y. Hou, F. Zuo, Q. Ma, C. Wang, L. Bartels, P. Feng, The Journal of Physical Chemistry C 116 (2012) 20132.

[35] P. Wang, B. Huang, X. Qin, X. Zhang, Y. Dai, J. Wei, M.-H. Whangbo, Angewandte Chemie International Edition 47 (2008) 7931.

[36] J. Li, X. Tian, M. Habasi, K. Chen, N. Pang, P. Hu, H.A. Aisa, CrystEngComm 14 (2012) 7621.

[37] L. Kuai, B. Geng, X. Chen, Y. Zhao, Y. Luo, Langmuir 26 (2010) 18723.

[38] P. Wang, B. Huang, X. Zhang, X. Qin, H. Jin, Y. Dai, Z. Wang, J. Wei, J. Zhan, S. Wang, J. Wang, a.M.-H. Whangbo, Chemistry-A European Journal 15 (2009) 1821.

[39] S. Ghosh, A. Saraswathi, S.S. Indi, S.L. Hoti, H.N. Vasan, Langmuir 28 (2012) 8550.

[40] J.F. Guo, B. Ma, A. Yin, K. Fan, W.L. Dai, Journal of Hazardous Materials 211–212 (2012) 77.

[41] N. Zhang, S. Liu, X. Fu, Y.-J. Xu, The Journal of Physical Chemistry C 115 (2011) 9136.

[42] J. Yu, G. Dai, B. Huang, The Journal of Physical Chemistry C 113 (2009) 16394.

[43] T. Morimoto, K. Suzuki, M. Torikoshi, T. Kawahara, H. Tada, Chemical Communications (2007) 4291.

[44] M.R. Elahifard, S. Rahimnejad, S. Haghighi, M.R. Gholami, Journal of the American Chemical Society 129 (2007) 9552.

[45] Y. Hou, X. Li, Q. Zhao, G. Chen, C.L. Raston, Environmental Science & Technology 46 (2012) 4042.

[46] D. Chen, T. Li, Q. Chen, J. Gao, B. Fan, J. Li, X. Li, R. Zhang, J. Sun, L. Gao, Nanoscale 4 (2012) 5431.

[47] X. Wang, S. Li, Y. Ma, H. Yu, J. Yu, The Journal of Physical Chemistry C 115 (2011) 14648.

[48] P. Wang, B. Huang, X. Qin, X. Zhang, Y. Dai, M.-H. Whangbo, Inorganic Chemistry 48 (2009) 10697.

[49] H. Zhang, X. Fan, X. Quan, S. Chen, H. Yu, Environmental Science & Technology 45 (2011) 5731.

[50] M. Zhu, P. Chen, M. Liu, ACS Nano 5 (2011) 4529.

[51] M. Zhu, P. Chen, M. Liu, Langmuir 28 (2012) 3385.

[52] Y. Tang, Z. Jiang, Q. Tay, J. Deng, Y. Lai, D. Gong, Z. Dong, Z. Chen, RSC Advances 2 (2012) 9406.

[53] D. Chen, S.H. Yoo, Q. Huang, G. Ali, S.O. Cho, Chemistry–A European Journal 18 (2012) 5192.

[54] J. Jiang, L. Zhang, Chemistry–A European Journal 17 (2011) 3710.

[55] M. Zhu, P. Chen, M. Liu, Journal of Materials Chemistry 21 (2011) 16413.

[56] C. An, R. Wang, S. Wang, X. Zhang, Journal of Materials Chemistry 21 (2011) 11532.

[57] L. Han, P. Wang, C. Zhu, Y. Zhai, S. Dong, Nanoscale 3 (2011) 2931.

[58] Y. Tang, Z. Jiang, G. Xing, A. Li, P.D. Kanhere, Y. Zhang, T.C. Sum, S. Li, X. Chen, Z. Dong, Z. Chen, Advanced Functional Materials (2013), http://dx.doi.org/10.1002/adfm.201203379.

[59] P. Hu, Y. Cao, Dalton Transactions 41 (2012) 8908.

[60] H. Xu, H. Li, J. Xia, S. Yin, Z. Luo, L. Liu, L. Xu, ACS Applied Materials & Interfaces 3 (2010) 22.

[61] M. Zhu, P. Chen, W. Ma, B. Lei, M. Liu, ACS Applied Materials & Interfaces 4 (2012) 6386.

[62] R. Dong, B. Tian, C. Zeng, T. Li, T. Wang, J. Zhang, The Journal of Physical Chemistry C 117 (2012) 213.

[63] E.C. Berglund, N.J. Kuklinski, E. Karagündüz, K. Ucar, J. Hanrieder, A.G. Ewing, Analytical Chemistry 85 (2013) 2841.

[64] T.R.M. De Beer, M. Wiggenhorn, R. Veillon, C. Debacq, Y. Mayeresse, B. Moreau, A. Burggraeve, T. Quinten, W. Friess, G. Winter, C. Vervaet, J.P. Remon, W.R.G. Baeyens, Analytical Chemistry 81 (2009) 7639.

[65] K.M. Phillips, J.K. Palmer, Journal of Agricultural and Food Chemistry 39 (1989) 1216.

[66] S. Ye, J. Feng, P. Wu, Journal of Materials Chemistry A 1 (2013) 3495.

[67] Z. Zhao, D. Chen, X. Jiao, The Journal of Physical Chemistry C 111 (2007) 18738.

[68] A.J. Svagan, P. Jensen, S.V. Dvinskikh, I. Furo, L.A. Berglund, Journal of Materials Chemistry 20 (2010) 6646.

[69] J. Ihli, A.N. Kulak, F.C. Meldrum, Chemical Communications 49 (2013) 3134.

[70] C. Wang, H. Liu, W. Yang, Journal of Materials Chemistry 22 (2012) 5281.

[71] Z. Wang, G.M. Kale, Q. Yuan, M. Ghadiri, RSC Advance 2 (2012) 9993.

[72] S.R. Mukai, H. Nishihara, S. Shichi, H. Tamon, Chemistry of Materials 16 (2004) 4987.

[73] Y. Gao, L. Song, P. Jiang, L.F. Liu, X.Q. Yan, Z.P. Zhou, D.F. Liu, J.X. Wang, H.J. Yuan, Z.X. Zhang, X.W. Zhao, X.Y. Dou, W.Y. Zhou, G. Wang, S.S. Xie, H.Y. Chen, J.Q. Li, Journal of Crystal Growth 276 (2005) 606.

[74] C.W. Xiao, H.T. Yang, C.M. Shen, Z.A. LI, H.R. Zhang, F. Liu, T.Z. Yang, S.T. Chen, H.J. Gao, Chinese Physics 14 (2005) 2269.

[75] J.T. Kloprogge, D. Wharton, L. Hickey, R.L. Frost, American Mineralogist 87 (2002) 623.

[76] D. Chen, Y. Sugahara, Chemistry of Materials 19 (2007) 1808.

[77] D. Chen, M. Liu, L. Yin, T. Li, Z. Yang, X. Li, B. Fan, H. Wang, R. Zhang, Z. Li, H. Xu, H. Lu, D. Yang, J. Sun, L. Gao, Journal of Materials Chemistry 21 (2011) 9332.

[78] M. Zayat, D. Einot, R. Reisfeld, Journal of Sol-Gel Science and Technology 10 (1997) 203.

[79] J. Jiang, L. Zhang, Chemistry – A European Journal 17 (2011) 3710.

[80] C.D. Wanger, W.M. Riggs, L.E. Davis, J.F. Moulder, G.E. Muilenberg, Handbook of X-ray Photoelectron Spectroscopy, Perkin-Elmer Corp., Physical Electronics Division, Eden Prairie, Minnesota, USA, 1979.

[81] Y. Marui, A. Kikuzawa, T. Kida, M. Akashi, Langmuir 26 (2010) 11441.

[82] L. Mohapatra, K. Parida, M. Satpathy, The Journal of Physical Chemistry C 116 (2012) 13063.

[83] T.S. Natarajan, K. Natarajan, H.C. Bajaj, R.J. Tayade, Industrial & Engineering Chemistry Research 50 (2011) 7753.

[84] M. Shang, W. Wang, S. Sun, J. Ren, L. Zhou, L. Zhang, The Journal of Physical Chemistry C 113 (2009) 20228.

[85] M. Mrowetz, W. Balcerski, A.J. Colussi, M.R. Hoffmann, The Journal of Physical Chemistry B 108 (2004) 17269.

[86] X. Yan, T. Ohno, K. Nishijima, R. Abe, B. Ohtani, Chemical Physics Letters 429 (2006) 606.

[87] G. Zhang, Y. Gao, Y. Zhang, Y. Guo, Environmental Science & Technology 44 (2010) 6384.